

Evidence for a Bose-Einstein condensate of excitons

Mathieu Alloing¹, Mussie Beian¹, Maciej Lewenstein^{1,2}, David Fuster³, Yolanda González³, Luisa González³, Roland Combescot^{4,5}, Monique Combescot⁶ and François Dubin^{1,6}

¹*ICFO-The Institute of Photonic Sciences, Av. Carl Friedrich Gauss 3, 08860 Castelldefels, Spain*

²*ICREA-Institució Catalana de Recerca i Estudis Avanats, Lluís Companys 23, 08010 Barcelona, Spain*

³*IMM-Instituto de Microelectrónica de Madrid (CNM-CSIC), Isaac Newton 8, PTM, E-28760 Tres Cantos, Madrid, Spain*

⁴*Laboratoire de Physique Statistique, Ecole Normale Supérieure, UPMC Paris 06, Université Paris Diderot, CNRS, 24 rue Lhomond, 75005 Paris, France*

⁵*Institut Universitaire de France, 103 boulevard Saint-Michel, 75005 Paris, France*

⁶*Institut des Nanosciences de Paris, CNRS and UPMC, 2 pl. Jussieu, 75005 Paris, France*

The demonstration of Bose-Einstein condensation in atomic gases at micro-Kelvin temperatures is a striking landmark¹ while its evidence for semiconductor excitons²⁻⁵ still is a long-awaited milestone. This situation was not foreseen because excitons are light-mass boson-like particles with a condensation expected to occur around a few Kelvins^{6,7}. An explanation can be found in the underlying fermionic nature of excitons which rules their condensation⁸. Precisely, it was recently predicted that, at accessible experimental conditions, the exciton condensate shall be "gray" with a dominant dark part coherently coupled to a weak bright component through fermion exchanges⁹. This counter-intuitive quantum condensation, since

excitons are mostly known for their optical activity, directly follows from the excitons internal structure which has an optically inactive, i.e., dark, ground state⁸. Here, we report compelling evidence for such a "gray" condensate. We use an all-optical approach in order to produce microscopic traps which confine a dense exciton gas that yet exhibits an anomalously weak photo-emission at sub-Kelvin temperatures. This first fingerprint for a "gray" condensate is then confirmed by the macroscopic spatial coherence and the linear polarization of the weak excitonic photoluminescence emitted from the trap, as theoretically predicted⁹.

Bose-Einstein condensation of semiconductor excitons has received a considerable attention since its theoretical prediction ²⁻⁵ in the 1960's. Unlike most commonly studied bosonic atoms⁶, the exciton composite nature plays a key role in their condensation. In semiconductor quantum wells, excitons are made of spin ($\pm 1/2$) electrons and "spin" ($\pm 3/2$) holes. These carriers mainly interact through attractive intraband Coulomb processes. Weak interband valence-conduction Coulomb processes also exist, but only for optically active, or "bright", excitons with total spin (± 1) made of ($\pm 3/2$) holes and ($\mp 1/2$) electrons. These (repulsive) interband processes bring the energy of bright excitons above the one of "dark" excitons with total spin (± 2) made of ($\pm 3/2$) holes and ($\pm 1/2$) electrons. As a result, Bose-Einstein condensation of excitons must occur within the low energy dark states ^{8,10}. This feature, which makes exciton condensation hard to evidence by conventional optical means, could be the reason why unambiguous signatures of exciton condensates have not been given yet, despite several decades of active experimental research. By contrast, the excitonic component of a polariton being by construction coupled to light, polariton condensation can be studied through photoluminescence, which recently led to remarkable

experiments^{11–14}.

While in the very dilute regime the exciton condensate must be completely dark, no matter how small the energy difference between dark and bright states is ⁸, it was recently shown⁹ that at sufficiently large density, carrier exchange between bright and dark excitons brings a coherent bright component to the condensate which becomes "gray". Such a coherence between dark and bright excitons is very similar to what occurs in the well known phases of superfluid ³He (see e.g. Ref.¹⁵), and in the more recent spinor condensates of ultracold atomic Bose gases¹⁶, where components of these superfluids corresponding to different internal degrees of freedom coexist and are coherent. This coherent coupling allows probing the exciton condensate through the photoluminescence of its bright part. As the bright component is very small, the photoluminescence signal is very weak. Nevertheless, it shall unveil the existence of a dense population of dark excitons, the spatial coherence of the condensate and its internal "spin" structure through the polarisation of the emitted light. In semiconductor quantum wells, the dark nature of exciton Bose-Einstein condensation has been overlooked until very recently^{8,10}, most probably because the splitting between bright and dark states is small compared to the thermal energy at critical temperature. Here, we present compelling experimental evidence for a "gray" Bose-Einstein condensate of excitons^{8,9} through the experimental observation of all its theoretically predicted characteristics.

We study excitons confined in a 25 nm wide GaAs single quantum well embedded in a field-effect device with an electrical polarization keeping electrons and holes well apart. As the electron and hole wave functions have a small overlap, these dipolar excitons have a long radiative

lifetime (~ 20 ns) and a rather large energy splitting between bright and dark states (~ 20 μ eV, see Ref. ^{18,19}). The electrical polarisation also ensures a repulsive effective exciton-exciton interaction which prevents the formation of biexcitons at the typical density n_c where Bose statistics becomes dominant ($n_c \simeq m_X k_B T / \hbar^2 \sim 10^{10}$ cm⁻² for 2D excitons with mass m_X at 1K).

We use a pump laser ($\lambda_{\text{pump}}=641.5$ nm) with an energy above the AlGaAs barriers of the quantum well in order to create a dense and well thermalised exciton gas. For such laser excitation photo-injected electrons and holes are captured by the quantum well with different efficiencies^{20,21}: a region richer in holes is formed around the laser excitation, itself surrounded by an electron-rich domain resulting from both the photo-current passing through our device and the modulation doping of the structure (see Fig. 1.A). In this landscape, dipolar excitons are created through the Coulomb interaction between photo-injected electrons and holes, the exciton transport being somewhat complicated by the ambipolar diffusion of excess carriers which screen the external field applied through our top gate electrode.

Figures 1.C and 1.D show the photoluminescence emission 10 ns after the pump pulse at 350 mK and 7K respectively. Both reveal a pattern characteristic of the charge separation existing in the quantum well, namely a macroscopic exciton ring formed a few tens of microns away from the pump excitation^{22,23}. Figures 1.E and 1.F show the exciton confinement potential together with the profile of the exciton density for these measurements. They are both deduced from a weak probe pulse which injects a very dilute exciton cloud after the pump pulse. Note that this probe beam is tuned well below the bandgap of the AlGaAs barriers ($\lambda_{\text{probe}}=790$ nm) in order to bring

essentially no perturbation²⁴. Excitons injected by the probe beam emit a photoluminescence at an energy $E_X \simeq (\vec{d} \cdot \vec{F}_{\text{screen}} + u_0 n_X)$. The first term corresponds to the energy increase of a single exciton resulting from the screening field $\mathbf{F}_{\text{screen}}$ induced by excess carriers, $d \approx e \cdot 15$ nm being the excitonic dipole moment¹⁷. The second term, where n_X is the exciton density and u_0 a parameter given by the geometry of our heterostructure²⁵, corresponds to the energy increase resulting from repulsive exciton-exciton interactions. By sending the probe pulse 100 ns after extinction of the pump, i.e. when all excitons injected by the pump have recombined, we directly map the excitons confinement as for very small exciton densities E_X reduces to $E_X^{(\text{probe})} = \vec{d} \cdot \vec{F}_{\text{screen}}$. We can estimate the density profile of excitons produced by the pump excitation by sending a probe pulse 10 ns after extinction of the pump as E_X reduces then to $E_X^{(\text{pump})} = (E_X^{(\text{probe})} + u_0 n_X)$. This pump-probe spectroscopy then allows us to extract the whole exciton density injected by the pump pulse, n_X , including dark and bright excitons, a crucial ingredient to signal a "gray" condensate.

Figures 1.E-F show the profile of the exciton confinement through $E_X^{(\text{probe})}$. It displays a maximum at the pump laser spot, then slowly decreases with the distance to the laser excitation before an abrupt decrease just before the region where the ring is formed. This is physically reasonable because the ring is expected to be located at the interface between the electron-rich and hole-rich domains where the near absence of excess carriers leads to a minimum screening. Most importantly, our measurements reveal at 350 mK that an electrostatic trap, i.e. a local minimum of $E_X^{(\text{probe})}$, is spontaneously formed in the vicinity of the ring (see Fig. 1.E). This potential confines dipolar excitons which are high-field seekers, i.e., attracted by strong field regions. We note that the exciton trap is not homogeneous along the circumference of the ring, i.e., it is not identical on

opposite sides (see Fig. 1.E). Its depth can be as large as $\simeq 1.2$ meV at 350 mK, an increase of the bath temperature leading to a reduction or a total suppression of the trap (Fig. 1.F).

We evaluate the exciton density by comparing $E_X^{(\text{pump})}$ to $E_X^{(\text{probe})}$. Figure 1.E shows at 350 mK that across the emission $E_X^{(\text{pump})}$ is blueshifted compared to $E_X^{(\text{probe})}$. This reveals that the pump pulse creates a dense exciton gas ($n_X \sim 10^{10} \text{ cm}^{-2}$ for a blueshift $(E_X^{(\text{pump})} - E_X^{(\text{probe})}) \sim 1 \text{ meV}$). More strikingly, we also note that $E_X^{(\text{pump})}$ is almost constant in the region of the ring (Fig. 1.E), unlike at 7K (Fig. 1.F). This reveals that dipolar excitons completely fill the trap spontaneously formed in the vicinity of the ring. The experimental blueshift (1.2 meV around the position $-25 \mu\text{m}$ in Fig. 1.E) leads to an exciton density $\sim 2 \cdot 10^{10} \text{ cm}^{-2}$ across the entire trap^{25–27}. At the same time, the photoluminescence intensity is reduced by more than ten fold between the positions (-25) and $(-31) \mu\text{m}$. At the latter position, the excitonic population then dominantly consists of optically inactive, i.e. dark, excitons. The dense but nearly dark exciton gas, highlighted by the gray area in Fig. 1.E, can only be explained by the formation of a condensate which acts as a sink and captures most of the excitons, this condensate being nearly dark, or "gray". Indeed, in the absence of a condensate, i.e. in the classical regime, the dark and bright populations should be very similar, because the dark-bright energy splitting ($\sim 20 \mu\text{eV}$) is smaller than the thermal energy ($\sim 30 \mu\text{eV}$ at our lowest bath temperature). This would lead to a much stronger photoluminescence than the one we observe. Such a conclusion is further supported by the spectral profile of the photoluminescence which is essentially identical on the brightest part of the ring and $6 \mu\text{m}$ outside¹⁷, fully coherent with the fact that the total exciton density stays unchanged throughout this region. Finally, Fig. 1-F shows that at higher temperatures we no longer find the spectral signature of a "gray" condensate. We wish

note that the specific position where the condensate is formed certainly is the result of a complex hydrodynamical diffusion, dipolar excitons experiencing a chute from the pump laser spot to the trapping region, while cooling at the same time.

To unambiguously confirm the formation of a "gray" condensate at sub-Kelvin bath temperatures, we further study the first order spatial coherence $|g^{(1)}|$ of the photoluminescence¹⁷ since the light emitted by the bright part of the condensate reflects its long-range order. The classical regime is distinguished from the quantum regime through its spatial coherence^{28,29}, the classical coherence length being of the order of the de Broglie wavelength ($\lambda_{dB} \sim 100$ nm at sub-Kelvin temperatures). We experimentally assess the coherence length of bright excitons by using an actively stabilized Mach-Zehnder interferometer. One arm of the interferometer displaces the photoluminescence laterally by $\delta_x = 1.5 \mu\text{m}$ with respect to the second arm; it also tilts it vertically, so that output interference fringes end up aligned horizontally^{2,17}. By scanning the phase of the interferometer, we reconstruct point by point the amplitude of the interference contrast. This allows us to draw the map of the emission first order spatial coherence from which we deduce¹⁷ the exciton coherence length ξ .

Figure 2 shows $|g^{(1)}|$ in the ring region. At high temperature ($T_b = 7\text{K}$ in Fig. 2.D), the interference contrast does not significantly vary across the emission, staying approximately equal to 10-15 % which is the background value of our interference contrast¹⁷. This leads to a coherence length $\xi \lesssim 200$ nm. At lower temperature ($T_b = 370$ mK in Fig. 2.C), the interference contrast exhibits a pattern correlated with the spatial profile of the photoemission in a way which again

reveals a "gray" condensate. Indeed, Fig. 3.A shows that the interference contrast is minimal ($\sim 10\%$) in the brightest part of the ring while, in the outer region where the photoluminescence intensity is strongly decreased, $|g^{(1)}|$ can reach $\approx 40\%$ which is above half the auto-correlation value (70% for $\delta_x = 0$). This shows that the observed bright excitons with a coherence length $\xi \sim 1.5 \mu\text{m}$ one order of magnitude larger than the de Broglie wavelength, belong to the condensate. The variation of the excitonic coherence as a function of the bath temperature moreover shows that non-classical correlations become dominant below a critical temperature $\sim 2\text{K}$, the coherence length abruptly increasing from near classical to non-classical values (see Fig. 3.C).

In order to obtain further insight into the internal structure of a gray condensate, we filter the polarization of the photoluminescence. In a "gray" condensate, dark and bright states are coupled by carrier exchanges⁹ or other coupling processes as suggested recently^{2,31–33}. Since the lowest energy for degenerate (± 1) or (± 2) states is obtained for a linear polarisation, due again to carrier exchanges⁸, a "gray" condensate must exhibit a linearly polarized photoluminescence. And indeed, Fig. 4.B shows at 370 mK that the photoluminescence is mostly polarized linearly in the outer region of the ring where macroscopic coherence is also observed (Fig. 3.C) – the degree of circular polarization being far smaller (see Fig.4.C). In the inner region of the ring, we also observe a linear polarization, but along the orthogonal direction. These observations contrast with recent studies performed in double quantum well heterostructures where dipolar (spatially indirect) excitons exhibit correlated patterns having both linear and circular polarizations³⁴. These patterns have been interpreted in terms of coherent exciton transport and spin-orbit coupling^{2,32,33}. Our experiments, which do not reveal these patterns, are performed in a single quantum well with

a dark-bright energy splitting much larger than in bilayer heterostructures. Since this splitting plays a key role in selecting the specific condensate which is formed, it is reasonable to think that experiments performed in single and double quantum wells probe different regimes.

As a last remark, one might wonder if our essentially two-dimensional geometry would not dramatically affect Bose-Einstein condensation. This is not so because condensation occurs in small regions which stabilizes the condensate¹. In addition, phase fluctuations, responsible for the main qualitative differences between 2D and 3D systems¹, are then quenched. Hence the condensate should be fairly similar to a 3D condensate.

1. *“Bose-Einstein Condensation”*, L.P. Pitaevskii, S. Stringari (Oxford university Press, 2003)
2. S.A. Moskalenko, Fiz. Tverd. Tela (Leningrad) **4**, 276 (1962)
3. J. M. Blatt et al., Phys. Rev. **126**, 1691 (1962)
4. L.V. Keldysh and YuV. Kopaev, Sov. Phys. Solid State **6**, 2219 (1965)
5. L.V. Keldysh and A.N. Kozlov, Sov. Phys. JETP **27**, 521 (1968)
6. *“Bose-Einstein condensation”*, Eds. A. Griffin, D. W. Snoke, S. Stringari (Cambridge Univ. Press, 1995)
7. *“Bose-Einstein Condensation of Excitons and Biexcitons”*, S.A. Moskalenko, D. W. Snoke, (Cambridge Univ. Press, 2000)
8. M. Combescot, O. Betbeder-Matibet, R. Combescot, Phys. Rev. Lett. **99**, 176403 (2007)
9. R. Combescot, M. Combescot, Phys. Rev. Lett. **109**, 026401 (2012)
10. M. Combescot, M.N. Leuenberger, Solid State Comm. **149**, 567 (2009)
11. H. Deng et al., Science **298**, 199 (2002)
12. J. Kasprzak et al., Nature **443**, 409 (2006)
13. R. Balili et al., Science **316**, 1007 (2007)
14. E. Wertz et al., Nat. Phys. **6**, 860864 (2010)
15. A.J. Leggett *Quantum Liquids* (Oxford. Univ. Press, 2006)

16. D.M. Stamper-Kurn, M. Ueda, Rev. Mod. Phys. **85**, 1191 (2013)
17. see Supplementary Informations
18. E. Blackwood et al., Phys. Rev. B **50**, 14246 (1994)
19. A.V. Gorbunov, V.P. Timofeev, Sol. Stat. Comm. **157**, 6 (2013)
20. L. V. Butov et al., Phys. Rev. Lett **92**, 117404 (2004)
21. R. Rapaport et al., Phys. Rev. Lett **92**, 117405 (2004)
22. L.V. Butov et al., Nature **418**, 751 (2002)
23. D.W. Snoke et al., Nature **418**, 754 (2002)
24. M. Alloing, A. Lemaitre, E. Gallopin, F. Dubin, Sci. Rep. **3**, 1578 (2013)
25. A. L. Ivanov, E. A. Muljarov, L. Mouchliadis, and R. Zimmermann, Phys. Rev. Lett. **104**, 179701 (2010)
26. C. Schindler and R. Zimmermann, Phys. Rev. B **78**, 045313 (2008)
27. B. Laikhtman. and R. Rapaport, Phys. Rev. B **80**, 195313 (2009)
28. M. Naraschewski and R. J. Glauber, Phys. Rev. A **59**, 4595 (1999)
29. I. Bloch, T. W. Haensch, T. Esslinger, Nature **403**, 166 (2000)
30. A.A. High et al., Nature **483**, 584 (2012)
31. M. Ali Can and T. Hakioglu, Phys. Rev. Lett. **103**, 086404 (2009)

- 32. M. Matuszewski et al., Phys. Rev. B **86**, 115321 (2012)
- 33. D.V. Vishnevsky et al., Phys. Rev. Lett. **110**, 246404 (2013)
- 34. A.A. High, et al., Phys. Rev. Lett. **110**, 246403 (2013)

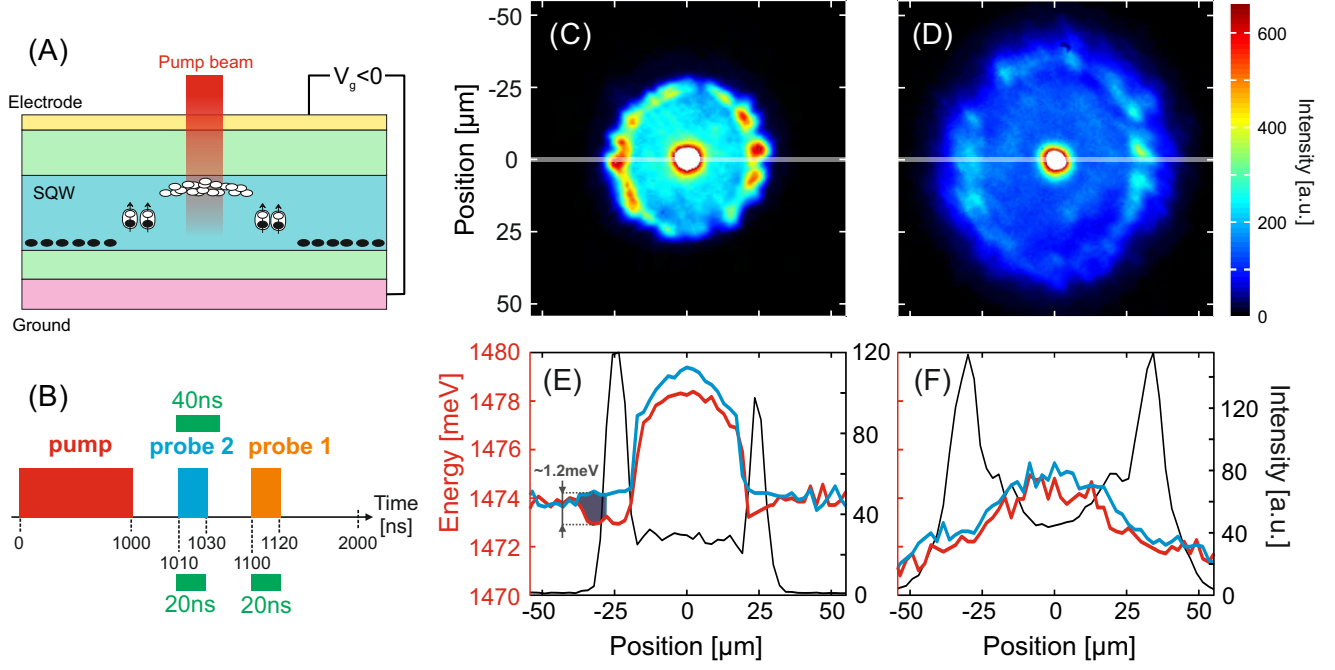


Fig. 1. (A): Sketch of our field-effect device: a pump beam excites a wide single quantum well (SQW) and produces a region rich in holes (open circles) around the laser spot, surrounded by a region rich in electrons (filled circles). These excess charges screen the electric field imposed by the potential V_g applied on the top electrode of the device. (B): Schematic time sequence showing pump and probe pulses together with the intervals during which our experimental results are recorded (green). (C-D) Real photoluminescence image recorded in a 40ns long time interval, starting 10 ns after extinction of the pump excitation, at 350 mK (C) and at 7K (D). (E-F) Spatial profiles of the excitonic confinement deduced from the $E_X^{(\text{probe})}$ measured in the "probe 1" pulse (red line) together with the exciton blueshift deduced from $E_X^{(\text{pump})}$ measured during the "probe 2" pulse (blue line). These profiles are taken along the white straight lines indicated in (C-D). The solid black lines in (E-F) show the profiles of the photoluminescence intensity. In (E) the gray region underlines a large exciton density at 350 mK in a region of anomalously weak photolumi-

nescence. It reveals the existence of a "gray" exciton condensate.

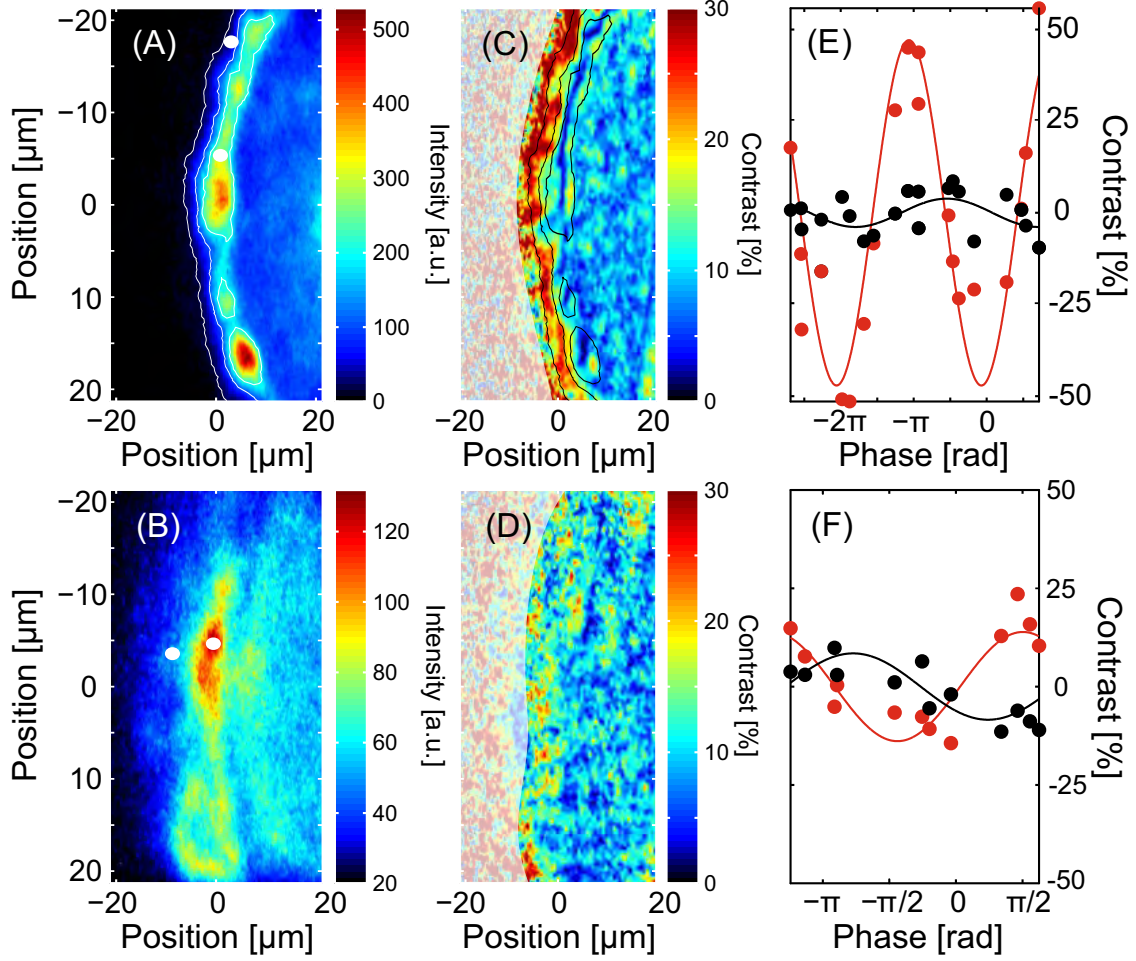


Fig. 2. (A-B): Photoluminescence taken from the same position of the ring at 370 mK (A) and at 7K (B). (C-D): Map of the interference contrast for $\delta_x = 1.5 \mu\text{m}$ at 370 mK (C) and at 7K (D). The shaded white area masks the region where the interference contrast can not be accurately measured because the photoluminescence intensity is too weak. (E-F): Variation of the interference contrast, at 370 mK (E) and at 7 K (F), as a function of the interferometer phase. Data are taken at the position of the ring (black) and 5 μm outside the ring (red). The white circles in (A) and (B) show these two positions.

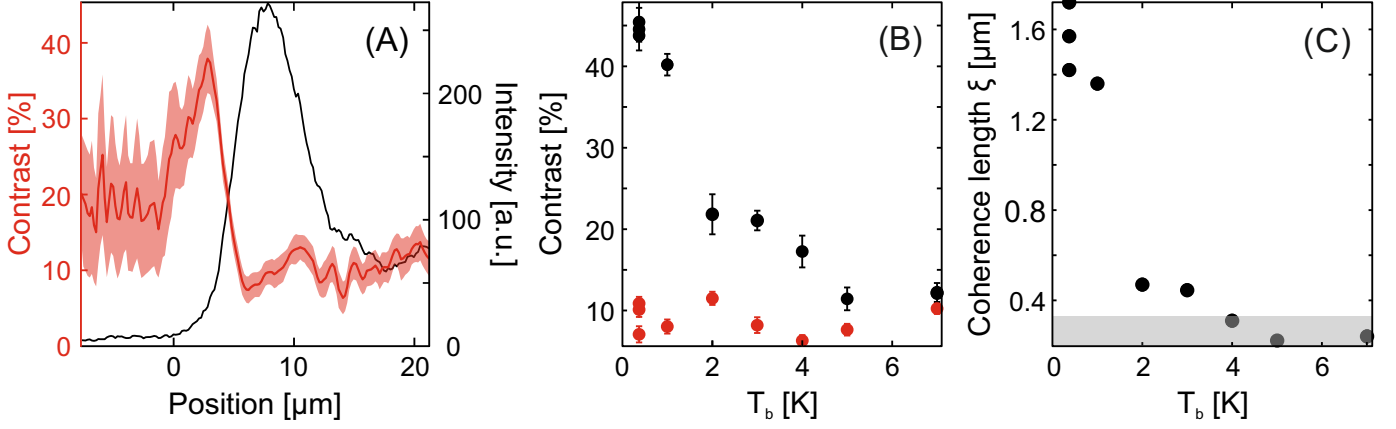


Fig. 3. (A): Intensity (dark) and interference contrast (red) of the photoemission across the fragmented ring at 370 mK. The red area shows the relative error in our measurements. The two vertical straight lines underline the maximum of the emission, i.e., the position of the ring, and the maximum of the interference contrast where the intensity is reduced by 10-fold. (B): Interference contrast for $\delta_x=1.5 \mu\text{m}$ as a function of the bath temperature T_b , taken $5 \mu\text{m}$ outside the ring (black) and at the position of the ring (red). (C) Coherence length as a function of the bath temperature measured $5 \mu\text{m}$ outside of the ring. The gray area shows the limit of our experimental resolution.

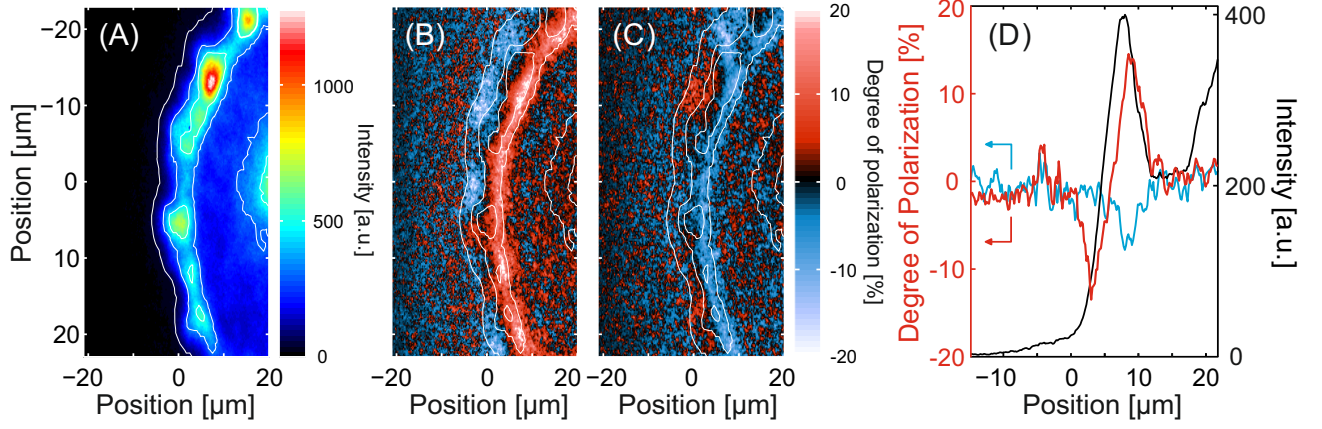


Fig. 4. Exciton ring at 370 mK (A). (B-C): Pattern of linear (B) and circular (C) polarizations at 370 mK. In (C), the blue and red colors are associated to σ^+ and σ^- polarized light respectively. In (B), we see that the photoemission is mostly linearly polarized in the outer region of the ring where extended spatial coherence is observed. (D): Degree of linear (red) and circular (blue) polarization of the photoluminescence at 370 mK. The solid dark line shows the intensity profile of the emission.

Supplementary Informations

Experimental details and sample structure

Our sample is schematically shown in Figure S1. It consists of a 1 μm thick field-effect device with an embedded 250 \AA wide GaAs quantum well. The quantum well is surrounded by $\text{Al}_{0.3}\text{Ga}_{0.7}\text{As}$ barriers incorporating a ten-period (2/2 nm) GaAs/ $\text{Al}_{0.3}\text{Ga}_{0.7}\text{As}$ superlattice. The quantum well is placed 900 nm below a millimeter wide semi-transparent gate electrode deposited on the surface of the sample. In our experiments, this electrode is biased at a constant voltage $V_g \sim -4.7$ V with respect to the n -doped sample substrate that is grounded. Our field-effect device is mounted in a ^4He - ^3He cryostat, which limits the optical resolution of our experiments to ≈ 1.5 μm due to mechanical vibrations. Let us note that this value refers to the measured full-width at half maximum of our gaussian-shaped point spread function.

Figure S2.B presents typical photoluminescence spectra emitted at the position of the ring at low (350 mK) and high (7K) bath temperatures. One notes that the emission spectrum narrows and acquires a well defined profile as the bath temperature is lowered. Precisely, at 350 mK it is made of two narrowband lines at an energy depending linearly on the gate voltage applied on our top electrode (see Figure S2.C). This reveals that these two emissions result from the recombination of quasi-particles with an electric dipole moment $\sim 15(3)$ nm, i.e. as expected for dipolar excitons confined in our electrically biased quantum well of 25 nm width. More interestingly, we also show that the intensity ratio between these two emissions depends strongly on the position on our sample: Figure S2.A shows that the high energy line dominates the spectrum in the vicinity of the

ring where charge neutrality is best fulfilled. On the other hand, the ratio is essentially even in the inner region of the ring which is rich in holes. This leads us to attribute the high energy component of the spectrum to the radiative recombination of dipolar excitons while the line at lower energy is attributed to the interaction between neutral excitons and excess carriers, e.g. holes in the inner region of the ring (a more quantitative analysis of the emission spectrum is beyond the scope of the present work and will be actually discussed elsewhere). Finally, we also display in Fig. S2.A the photoluminescence spectrum emitted at the position of the ring and 6 μm outside. These two emission profiles are essentially identical, e.g. the spectral linewidth is unchanged between these two positions whereas the photoluminescence intensity varies by over one order of magnitude. This observation further confirms our conclusion of a weakly varying exciton density in the electrostatic trap formed spontaneously in the vicinity of the ring. Otherwise the photoluminescence spectral width would vary as the result of homogeneous broadening which reflects the density of dipolar excitons¹.

First order coherence of the photoluminescence

To quantify the first order coherence of dipolar excitons, we magnify and spatially filter the photoluminescence emitted in the ring region. This part of the emission is directed towards a Mach-Zehnder interferometer with a path length difference between its two arms that is actively stabilized. This allows us to control the phase ϕ of the output interference signal with a $\approx (\pi/10)$ accuracy. The magnified photoluminescence is then split between the arms 1 and 2 of the interferometer, and a vertical tilt angle (α) is introduced between the outputs of the two arms. Hence,

interference fringes are aligned horizontally^{2,3}, α being set such that the interference period is $\approx 4 \mu\text{m}$. In this situation, the outputs produced by the two arms are laterally shifted by δ_x while the path length difference remains close to zero. This allows us to derive the degree of spatial coherence of the bright excitons.

The output of our interferometer, I_{12} , can be modelled as

$$I_{12}(\mathbf{r}; \delta_x) = \langle |\psi_0(\mathbf{r}, t) + e^{i(q_\alpha y + \phi)} \psi_0(\mathbf{r} + \delta_x, t)|^2 \rangle_t,$$

where $\psi_0(\mathbf{r})$ is the photoluminescence field which reflects the bright excitons wave function, $\langle \dots \rangle_t$ denotes the time averaging, $\mathbf{r}=(x,y)$ is the coordinate in the plane of the quantum well while $q_\alpha=2\pi\lambda^{-1}\sin(\alpha)$ where λ is the emission wavelength. By recording individually the output of the two arms, I_1 and I_2 , we can compute interferograms or normalized interference patterns $I_{\text{int}}=(I_1-I_2)/2\sqrt{I_1 I_2}$ which reveal the first order coherence function of indirect excitons, defined as

$$g^{(1)}(\mathbf{r}; \delta_x) = \frac{\langle \psi_0^*(\mathbf{r}, t) \psi_0(\mathbf{r} + \delta_x, t) \rangle_t}{(\langle |\psi_0(\mathbf{r}, t)|^2 \rangle_t \langle |\psi_0(\mathbf{r} + \delta_x, t)|^2 \rangle_t)^{1/2}}.$$

Indeed, $I_{\text{int}}(\mathbf{r}; \delta_x) = \cos(q_\alpha y + \phi + \phi_{\mathbf{r}}) |g^{(1)}(\mathbf{r}; \delta_x)|$ where $\phi_{\mathbf{r}}$ is the phase of $g^{(1)}$. Hence, normalized interferences have a visibility controlled by the degree of spatial coherence of bright excitons, while the position of the interference fringes reveals the phase of $g^{(1)}$, i.e., the phase difference between the interfering excitonic wave functions.

In Figure S3, we present some interferograms used to study the spatial coherence of dipolar excitons (Figure 2). Varying the phase of the interferomer, ϕ , we deduce $|g^{(1)}(\mathbf{r}; \delta_x)|$ as shown in Fig. 2.C-D.

Our experiments show regions where the intensity of the photoluminescence is weak while the degree of spatial coherence is large. To quantify it, we use a standard numerical routine to fit the variation of I_{int} as a function of ϕ . The fitting error becomes large when the intensity of the photoluminescence emission reaches 1% of its maximum at the ring position. This corresponds to ≈ 10 -20 counts on our photo-detector. Such a limitation is illustrated in Fig. S4 which presents the map of the interference contrast together with its relative error for the experiment shown in Fig. 2.C. We see that, in the outer region of the ring, the interference contrast is large and measured with a good precision while, for lower intensities, the fitting error is of the same order as the contrast we extract. To produce "simple" maps of the photoluminescence spatial coherence (Figure 2.C-D), we discard the regions where the fitting error is large.

Finally, to extract the bright exciton coherence length ξ quantitatively, we model the variation of $|g^{(1)}|$ by the convolution between a Gaussian profile with a $1.5 \mu\text{m}$ full-width at half-maximum and an exponential decay^{4,5}. The former function accounts for our instrumental resolution while the latter function provides the theoretical variation of $g^{(1)}$, namely $|g^{(1)}(\delta_x)| \propto e^{-\delta_x/\xi}$. For our interferometric setup, we calibrate the variation of $|g^{(1)}|$ as a function δ_x in previous experiments³. The coherence length of bright excitons ξ is then obtained from the interference contrast at $\delta_x=1.5 \mu\text{m}$ (Fig. 2.H).

Limitation of shift interferometry

Semkat et al. have recently proposed theoretically that a sharp enough photoluminescence pattern can lead to a significant visibility in shift-interferometry, even for a spatially incoherent

emission source ⁵. To discard such effects in our experiments, we simulate the ring photoluminescence (which is the sharpest pattern of the emission we study) with the incoherent photoluminescence emitted by the n-doped GaAs substrate of our field-effect device. For that, we excite the sample with a linear laser beam whose horizontal spatial linewidth is varied. As predicted by Semkat et al., we verify that the interference contrast is enhanced when the spatial width of the laser excitation is decreased. Precisely, we obtain a contrast up to $\sim 15\%$ for a photoluminescence with spatial extension $\sim 3.5\mu\text{m}$. Yet the visibility decreases rapidly when the photoluminescence broadens spatially. This is shown in Fig.S5 for a spatial extension $\sim 7.4\mu\text{m}$ which is slightly smaller than the spatial width of the ring at our lowest bath temperature. In this range, the interference contrast is everywhere less than 10% which sets the limit of our instrumental resolution, in good agreement with the interference contrasts we measure at high temperatures (see Fig. 3). Accordingly, we conclude that the $\sim 45\%$ interference visibility we observe at sub-Kelvin bath temperatures can not be explained by our instrumental resolution.

1. Z. Voros, D.W. Snoke, K. West and L. Pfeiffer, Phys. Rev. Lett. **103**, 016403 (2009)
2. A.A. High et al., Nature **483**, 584 (2012)
3. M. Alloing, D. Fuster, Y. Gonzalez, L. Gonzalez and F. Dubin, arXiv:1210.3176
4. M.M. Fogler et al., Phys. Rev. B **78**, 035411 (2008)
5. D. Semkat et al., Nano Lett. **12**, 5055 (2012)

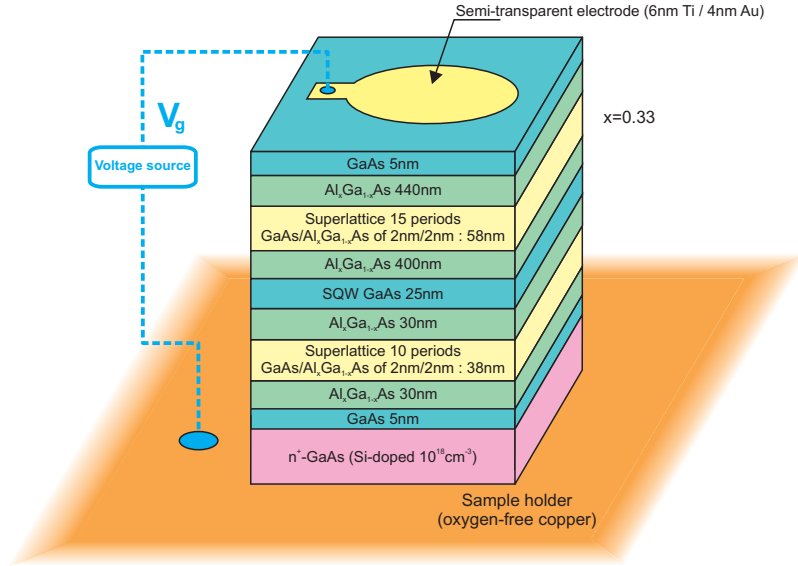


Fig. S1. Schematic representation of the field-effect device probed in our experiments.

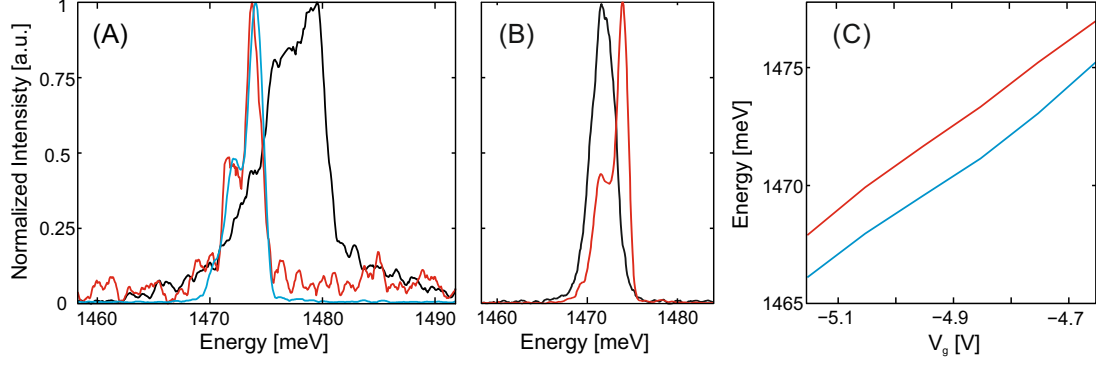


Fig. S2. (A): Normalized photoluminescence spectrum emitted at the position of the ring (blue), in the inner region of the ring (black) and 6 μm outside the ring where we identify the "gray" condensate (red). Beside a factor 20 in intensity this spectrum is essentially identical to the one emitted at the position of the ring. Data are all acquired at 350 mK. (B): Rescaled photoluminescence spectra emitted at the position of the ring at 350 mK (red) and at 7K (black). (C): Energy of the photoluminescence emitted at the position of the ring and as a function of the potential V_g applied onto the top gate of our field-effect device. The variation of the low and high energy components of the spectrum are displayed in blue and red respectively. From these linear variations we deduce an electrical dipole moment $\sim 15(3)$ nm for both lines at 350 mK.

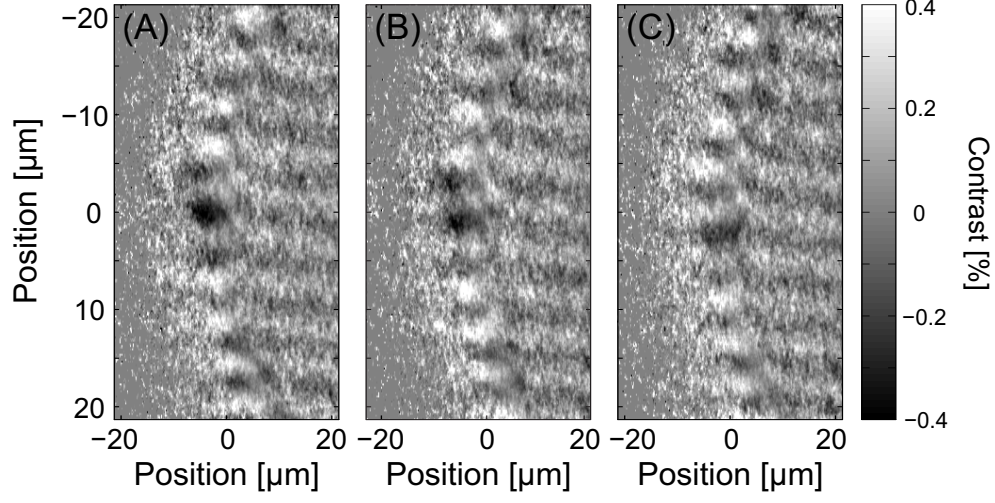


Fig. S3. (A-C): Normalized interference patterns I_{int} obtained for $\delta_x = 1.5 \mu\text{m}$. From (A) to (C), the phase of the interferometer ϕ are 0 , $\pi/2$, and π . From such interferograms, we compute the map of $|g^{(1)}|$ shown in Fig. 2.C. All measurements are realized at 370 mK by integrating in a 40 ns long time interval set 10 ns after extinction of a $1 \mu\text{s}$ laser excitation.

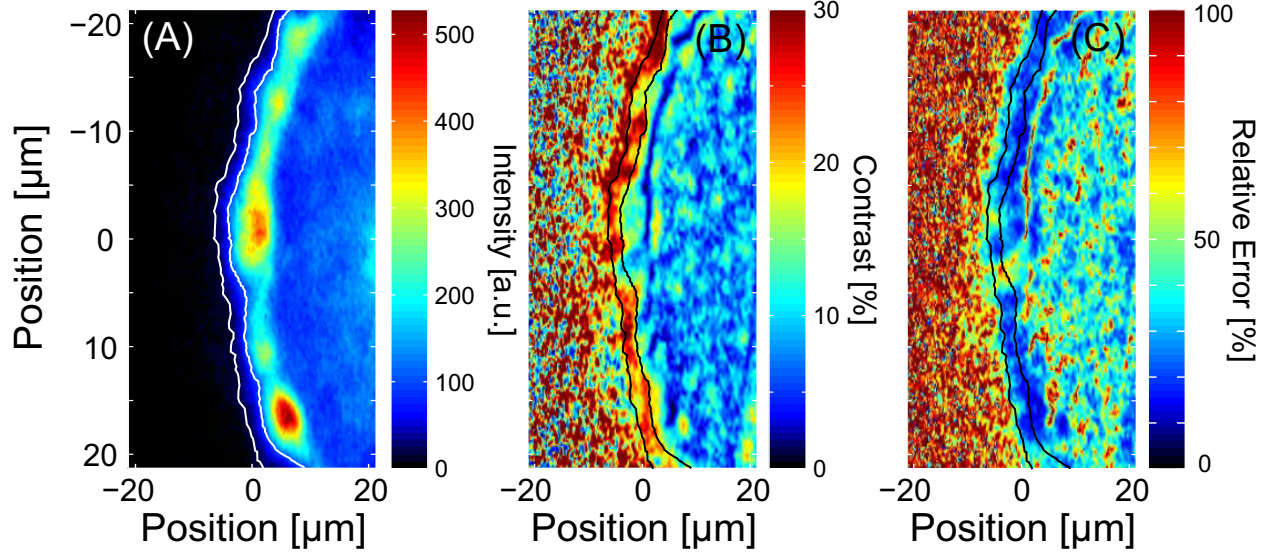


Fig. S4. (A): Photoluminescence emission in the region of the fragmented ring at 370 mK. This image is identical to the one shown in Fig.2.A. (B): Map of the interference contrast that we obtain by fitting point by point the variation of the interference signal as a function of ϕ . The relative error of the fit is displayed in (C) which shows that we can not extract the contrast with a sufficient accuracy for regions where the photoluminescence intensity is less than ≈ 20 counts. In (A-C), the two contour lines are iso-intensities where the emission is equal to 20 and 100 counts respectively. These underline the region where we observe macroscopic spatial coherence with high resolution.

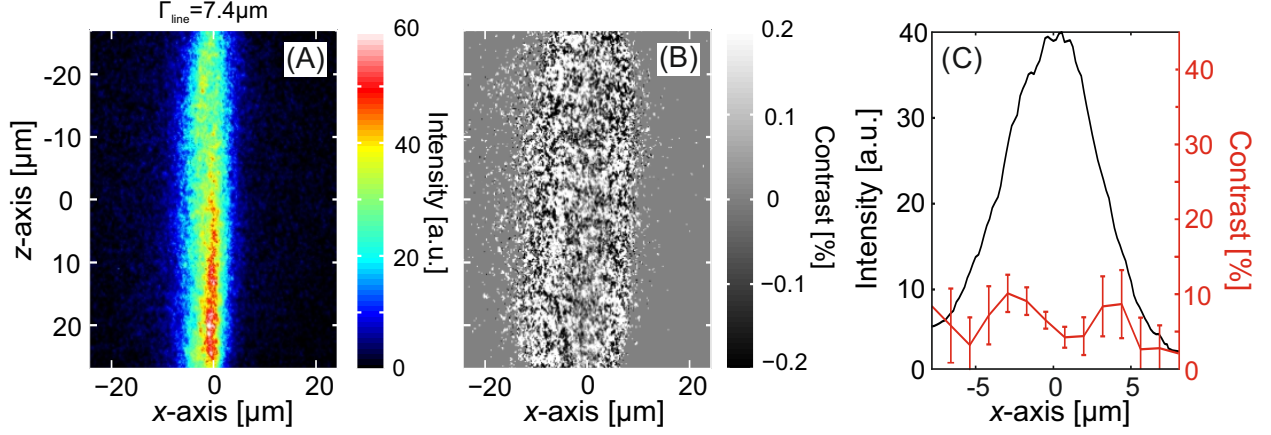


Fig. S5. (A): Photoluminescence emission of the n-doped GaAs substrate ($V_g = 0$) excited with a linear laser beam. The spatial width of the photoluminescence along the x -axis is $7.4\mu\text{m}$. (B) Normalized interferogram obtained with this incoherent photoluminescence pattern for a lateral shift of $\delta_x = 1.5\mu\text{m}$. (C) Intensity profile of (A) (black line) and spatially resolved contrast (red line), both along the x -axis. The contrast was obtained by fitting z -axis profiles of the interferogram with a cosine function for various positions on the x -axis. The intensity and contrast profiles are limited to $\sim 10\mu\text{m}$ on both sides of the origin of the horizontal axis, for larger distances, the intensity of the photoluminescence is too weak to resolve clear interferences. The ordinate scale of the interference contrast in (C) is set up to 45% in order to match Fig. 3 of the main text.